AIAA JOURNAL
Vol. 31, No. 1, January 1993

Spectral Element-Fourier Method for Transitional Flows in Complex Geometries

Cristina H. Amon*
Carnegie Mellon University, Pittsburgh, Pennsylvania 15213

An efficient spectral element-Fourier method is presented for the direct numerical simulation of transitional internal flows in complex geometries. This method is applied for the spatial discretization of the unsteady, incompressible, three-dimensional Navier-Stokes equations in the velocity-pressure formulation. The resulting discrete equations are solved by a semi-implicit method in time, where the nonlinear convective term is treated explicitly. Direct numerical simulations are performed to investigate the spatial structure and temporal evolution of two- and three-dimensional transitional flows in grooved channels.

I. Introduction

SPECTRAL methods have been used with success in analyzing complex flow phenomena in simple geometries. They have become the prevailing numerical method for three-dimensional direct simulation of transitional and turbulent shear flows. For instance, in the areas of hydrodynamic stability, transition, and turbulence, the accuracy and resolution of spectral techniques have allowed the understanding and simulation of Poiseuille flow,[1] Taylor vortex flow,[2] and shear layers.[3] A review of spectral methods in fluid dynamics is presented by Canuto et al.[4] However, until recently, only direct numerical simulations (DNS) of transitional and turbulent flows in simple geometries have been done using spectral techniques, mainly because a single, global expansion cannot represent flows in complex geometry or the transformed domain may introduce artificial singularities or boundary layers. Moreover, it is not advisable to use global spectral methods when the resolution requirements vary widely over the domain, since dense matrices are generated that are expensive to invert.

To overcome these difficulties, spectral domain decomposition techniques have been proposed where the computational domain is partitioned into subdomains or elements. Different techniques for interface patching have been implemented to match the solution along the common boundary of the elements.[4] One of these techniques is the spectral element method, introduced by Patera,[5] in which the interfacial continuity constraints are imposed via a variational formulation as in the p-type finite element method. It is interesting to note that the tendency in both finite difference and finite element methods has been to replace second-order by higher order schemes, whereas the trend in spectral techniques has been the replacement of a global approximation by local expansions defined only in a subdomain.

Spectral element methods are high-order, weighted-residual techniques that combine the generality and geometric flexibility of the low-order, h-type finite element schemes with the accuracy and rapid convergence rate of spectral expansions. They have proven particularly successful in simulating accurately two-dimensional flows[6-8] involving delicate phenomena with fine spatial scales and complex structures. Therefore, we propose to extend the spectral element method by combining it with Fourier expansions in the spanwise direction for direct numerical simulation of the time-dependent, three-dimensional Navier-Stokes equations in complex geometries with one homogeneous flow direction.

In this paper, we present the formulation and implementation of the spectral element-Fourier method. In Sec. II, the continuous problem and the governing equations are introduced. In Sec. III, the discrete formulation is presented, and the temporal and spatial discretizations are discussed. Finally, in Sec. IV, the numerical simulations of two- and three-dimensional transitional flows in grooved channels are presented.

II. Mathematical Formulation

We consider incompressible flows with constant properties, which are governed by the Navier-Stokes and mass conservation equations. If we denote by D the three-dimensional computational domain, and by ∂D the computational boundary surface, the governing dimensionless equations are written in the following form (in D):

$$\frac{\partial v}{\partial t} = v \times \omega - \nabla \tilde{\Pi} + R^{-1} \nabla^2 v \tag{1}$$

$$\nabla \cdot v = 0 \tag{2}$$

where $v(x, t) = u\hat{x} + v\hat{y} + w\hat{z}$ is the velocity; x and t represent space and time, respectively; $\tilde{\Pi}$ is the dynamic pressure $= p + \frac{1}{2}v^2$, and ω is the vorticity $= \nabla \times v$.

The boundary conditions are Dirichlet on solid walls, Neumann on outflow, and periodicity on homogeneous or fully developed directions. To illustrate the spectral element Fourier method, we consider the incompressible flow in the periodic grooved channel shown in Fig. 1. The velocities are nondimensionalized by $3V/2$, where V is the cross-channel average velocity, and the lengths are nondimensionalized by the channel half-height h. The Reynolds number is defined as $R = (3/2)Vh/\nu$. The flow is assumed to be periodic, fully developed in the streamwise direction x, and homogeneous in the spanwise

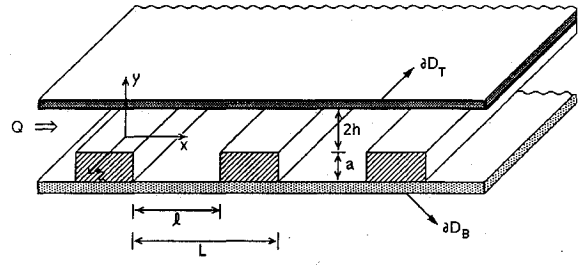

Fig. 1 Grooved-channel geometry, $L/h = 5$, $\ell/h = 3$, and $a/h = 1.68$.

Received May 8, 1991; presented as Paper 91-1608 at the AIAA 18th Computational Fluid Dynamics Conference, Honolulu, HI, June 24-26, 1991; revision received June 26, 1992; accepted for publication June 26, 1992.

*Assistant Professor, Department of Mechanical Engineering. Member AIAA

direction z. Based on the preceding assumption, the velocity boundary conditions are

$$v(x, t) = 0 \qquad \text{on } \partial D_s \tag{3}$$

$$v(x + nL, y, z, t) = v(x, y, z, t) \qquad \text{on } \partial D_p \tag{4}$$

where L is the geometric periodicity between grooves and n an integer periodicity index. For the pressure we require

$$\tilde{\Pi}(x, t) = -f(t)x + \Pi(x, t) \tag{5}$$

$$\Pi(x + nL, y, z, t) = \Pi(x, y, z, t) \tag{6}$$

where $f(t)$ is the driving pressure gradient. Since in complex geometry flows or transitional flows the pressure gradient is unknown, it is preferable to impose the volume flow rate $Q(t)$, defined as

$$Q(t) = \int_{-W}^{W} \int_{\partial D_B}^{\partial D_T} u(x_0, y, z, t)\, dy\, dz = \frac{8}{3} W \tag{7}$$

where $2W$ is the periodicity length in the spanwise direction.

III. Discretization

A. Temporal Discretization

The time-stepping procedure consists of a fractional scheme for the semidiscrete formulation of the time-dependent term in the Navier-Stokes equation. Intermediate velocities $\hat{v}$ and $\hat{\hat{v}}$, Eqs. (8–10), are computed in a way that the left-hand side yields $\partial v/\partial t$ whereas the right-hand side contains the contributions of the nonlinear, pressure, and viscous terms. The advantage of this time-splitting scheme is that it reduces the coupled system of Eqs. (1) and (2) into a system of separately solvable equations for the pressure and velocity enabling the application of different algorithms to different terms in the Navier-Stokes equations to obtain gains in efficiency. The error, due to the time-splitting scheme, scales as $[\mathcal{O}(\Delta t^2) + \mathcal{O}(\Delta t/R)]$ and restricts the time-step size in applications seeking to simulate time-dependent transitional flows. The nonlinear convective term, Eq. (8), is treated explicitly to decrease the computer time required per step because of the need to solve a boundary value problem at each time step. The viscous term, Eq. (10), is treated implicitly to avoid unreasonable time-step restrictions due to the stiffness of diffusion problems[9] and the high resolution of Chebyshev spectral approximations near the boundary of the elements.[10] The dynamic pressure Π is calculated in Eq. (11) so that the velocity satisfies the incompressible condition of Eq. (2) even though Π does not appear there. The time-stepping procedure is given by the following steps:

Nonlinear step:

$$\frac{\hat{v}^{n+1} - v^n}{\Delta t} = \sum_{i=0}^{2} \beta_i (v^{n-i} \times \omega^{n-i}) + f \qquad \text{in } D \tag{8}$$

Pressure step:

$$\frac{\hat{\hat{v}}^{n+1} - \hat{v}^{n+1}}{\Delta t} = -\nabla \Pi \qquad \text{in } D \tag{9a}$$

$$\nabla \cdot \hat{\hat{v}}^{n+1} = 0 \qquad \text{in } D \tag{9b}$$

$$\hat{\hat{v}} \cdot \hat{n} = 0 \qquad \text{on } \partial D \tag{9c}$$

Viscous step:

$$\frac{v^{n+1} - \hat{\hat{v}}^{n+1}}{\Delta t} = \frac{1}{R} \nabla^2 v^{n+1} \qquad \text{in } D \tag{10a}$$

subject to

$$v^{n+1} = 0 \qquad \text{on } \partial D_s \tag{10b}$$

$$v^{n+1}(x + nL, y, z) = v^{n+1}(x, y, z) \qquad \text{on } \partial D_p \tag{10c}$$

where the superscript n refers to time step, and the subscripts s and p refer to solid wall and periodicity, respectively. The first step, Eq. (8), represents the explicit treatment of the nonlinear convective term by a third-order Adams-Bashforth method, where the coefficients are $\beta_0 = 23/12$, $\beta_1 = -16/12$, and $\beta_2 = 5/12$. This scheme introduces low dispersion errors and contains a relatively large portion of the imaginary axis within the absolute stability region of the scheme.

In the second step, Eqs. (9a–9c), the effect of the pressure is included and incompressibility is satisfied. By taking the divergence of Eq. (9a) and imposing Eq. (9b), we obtain the following Poisson equation for the pressure:

$$\nabla^2 \Pi = \nabla \cdot \frac{\hat{v}^{n+1}}{\Delta t} \qquad \text{in } D \tag{11a}$$

This elliptic equation is then solved implicitly subject to

$$\nabla \Pi \cdot \hat{n} = \frac{\hat{v}^{n+1} \cdot \hat{n}}{\Delta t} \qquad \text{on } \partial D_s \tag{11b}$$

The imposition of an inviscid-type boundary condition, proposed first by Deville and Orszag,[10] introduces errors of $\mathcal{O}(\Delta t/R)$ that are important only at very low Reynolds number flows.

Finally, at the third fractional step, Eqs. (10a–10c), the viscous corrections are handled implicitly using a Crank-Nicolson scheme and the no-slip and periodic boundary conditions are imposed, giving

$$\left(\nabla^2 - \frac{2}{\Delta t} R\right)(v^{n+1} + v^n) = -\frac{2}{\Delta t} R(\hat{\hat{v}}^{n+1} + v^n) \qquad \text{in } D \tag{12a}$$

subject to

$$v^{n+1} = 0 \qquad \text{on } \partial D_s \tag{12b}$$

$$v^{n+1}(x + nL, y, z) = v^{n+1}(x, y, z) \qquad \text{on } \partial D_p \tag{12c}$$

The nonlinear convective term, treated explicitly, is the only source that imposes stability conditions for the scheme (Courant-Friedrich-Lewy condition number), since the pressure and viscous contributions are treated implicitly by Euler backward or Crank-Nicolson schemes, which are unconditionally stable, resulting in an efficient and robust inversion of the global system matrices. Consequently, the time-step size is constrained by both accuracy in the time-splitting formulation and stability of the explicit scheme. For high Reynolds number flows in the turbulent flow regime, the viscous term can be treated explicitly since stability conditions for the convective contributions, Eq. (8), are as severe as the ones for the diffusive contributions, Eqs. (10a–10c).

B. Spatial Discretization

Once we obtain the semidiscrete temporal equations, we proceed with the spatial discretization using a spectral element-Fourier decomposition of the computational domain. For a homogeneous geometry in the z direction, periodic boundary conditions and symmetry are consistent with the governing equations (1) and (2). Therefore, the velocity and pressure can be represented as two-dimensional (x, y) components with Fourier expansions in the homogeneous z direction,

$$\begin{bmatrix} u(x,t) \\ v(x,t) \\ w(x,t) \\ \Pi(x,t) \end{bmatrix} = \begin{bmatrix} u^{(2)}(x,y,t) \\ v^{(2)}(x,y,t) \\ w^{(2)}(x,y,t) \\ \Pi^{(2)}(x,y,t) \end{bmatrix} + \sum_{m=1}^{M} \begin{bmatrix} u_m(x,y,t)\cos(m\beta z) \\ v_m(x,y,t)\cos(m\beta z) \\ w_m(x,y,t)\sin(m\beta z) \\ \Pi_m(x,y,t)\cos(m\beta z) \end{bmatrix} \tag{13}$$

where β is the wave number in the spanwise direction. We use cosine and sine expansions instead of exponentials because of the symmetry in the z direction and the reality conditions of the velocity and pressure in the physical space. For the analysis of two-dimensional flows, the v_m are identically zero; for linear three-dimensional stability analysis, a single, infinitesimally small spanwise mode is included; and for three-dimensional flows, M is chosen so as to include all excited spanwise scales.

To impose the flow-rate condition $Q(t)$ in Eq. (7), let us assume for simplicity the flow direction to be the x direction (Fig. 1). Then, for incompressible flow, at station x_0,

$$Q(t) = \int\int u(x_0, y, z, t)\, dy\, dz = \int\int \left[u^{(2)}(x_0, y, t) + \sum_{m=1}^{M} u_m(x_0, y, t)\cos(m\beta z) \right] dy\, dz$$
$$= \int\int u^{(2)}(x_0, y, t)\, dy\, dz + \sum_{m=1}^{M} \int u_m(x_0, y, t)\, dy \int \cos(m\beta z)\, dz \qquad (14)$$

where

$$\int_{-W}^{W} \cos(m\beta z)\, dz = 0 \qquad m \neq 0$$

Therefore, only the mean streamwise velocity $u^{(2)}$ contributes to the net flow rate, obtaining

$$Q(t) = 2W \int_{\partial D_B}^{\partial D_T} u^{(2)}(x_0, y, t)\, dy = Q_{2D}(t) \cdot 2W \qquad (15)$$

It suffices to impose at any x_0 station

$$Q_{2D}(t) = \int_{\partial D_B}^{\partial D_T} u^{(2)}(x_0, y, t)\, dy = \frac{4}{3} \qquad (16)$$

which is done in a preprocessing stage, before the time-stepping procedure.

1. Fourier Expansions

The Fourier expansions, Eq. (13), are then inserted into the semidiscrete equations, Eqs. (8), (11), and (12). To demonstrate this procedure, we consider the elliptic operator corresponding to the pressure step, Eq. (11a), and substituting Eq. (13), we obtain

$$\sum_{m=1}^{M} (\nabla^2 - m^2\beta^2)\Pi_m \cos(m\beta z) = \frac{1}{\Delta t}\left(\sum_{m=1}^{M} \frac{\partial \hat{u}_m}{\partial x} + \frac{\partial \hat{v}_m}{\partial y} + m\beta \hat{w}_m \right)\cos(m\beta z) \qquad (17)$$

where $\nabla^2 = \partial^2/\partial x^2 + \partial^2/\partial y^2$ and Π_m are the Fourier coefficients for the spanwise direction. First, we follow a Galerkin approach in z, multiplying Eq. (17) by $\cos(k\beta z)$, integrating and applying orthogonality property to obtain the following equation for the Fourier coefficients Π_m[11]:

$$(\nabla^2 - m^2\beta^2)\Pi_m = \frac{1}{\Delta t}\left(\frac{\partial \hat{u}_m}{\partial x} + \frac{\partial \hat{v}_m}{\partial y} + m\beta \hat{w}_m \right) \qquad m = 1, 2, \ldots, M \qquad (18)$$

We can now proceed to discretize the two-dimensional components of the velocity and pressure in the x-y plane using a variational spectral element discretization.

2. Spectral Element Method

In the spectral element discretization, the computational domain is broken up into four-sided macroelements and each element is then isoparametrically mapped from the physical (x, y) space to the local (r, s) coordinate system. The geometry, pressure, and velocity are represented as a tensor product of high-order Lagrangian interpolants through Gauss-Lobatto Chebyshev collocation points, defined as

$$[x, v, \Pi](r, s) = \sum_{k=1}^{K} \sum_{i=0}^{N_1} \sum_{j=0}^{N_2} (x, v, \Pi)_{ij}^{k} h_i(r) h_j(s) \qquad (19)$$

where $h_i(r)$ and $h_j(s)$ are local Lagrangian interpolants that satisfy $h_i(\zeta_j) = \delta_{ij}$ at the local (r, s) coordinates, and δ_{ij} is the Kronecker delta symbol. The discrete space is defined in terms of the spectral element discretization parameters (K, N_1, N_2), where K is the number of spectral elements, and N_1 and N_2 are the degrees of the piecewise high-order polynomials in the r and s directions, respectively. To insure rapid convergence of the resulting expansions, the local and physical collocation points are chosen to be the Gauss-Lobatto Chebyshev points, defined as $x_j^i = -\cos \pi j/N^i$. Also, the choice of these collocation points enables us to use closed-form analytical expressions for the quadratures involved in the computations. The interpolants in Eq. (19) are expanded as

$$h_m(\zeta) = \frac{2}{N} \sum_{n=0}^{N} \frac{1}{\bar{c}_m \bar{c}_n} T_n(\zeta_m) T_n(\zeta) \qquad (20)$$

where $m = i, j$ and $\zeta = r, s$, and T_n are the Chebyshev polynomials defined as

$$T_n(\cos\theta) = \cos n\theta \qquad (21)$$

and

$$\bar{c}_m = \begin{cases} 1 & m \neq 0, N \\ 2 & m = 0, N \end{cases} \qquad (22)$$

In the numerical simulations presented in this paper, we choose the same resolution in both spatial directions, i.e., $N = N_1 = N_2$. However, in practice, this does not need to be the case.

To illustrate the spectral element discretization, we consider Eq. (18) corresponding to the pressure step discretized in the spanwise direction. To simplify the notation, let us set $g = (\partial \hat{u}_m/\partial x + \partial \hat{v}_m/\partial y + m\beta \hat{w}_m)/\Delta t$ since all of the variables

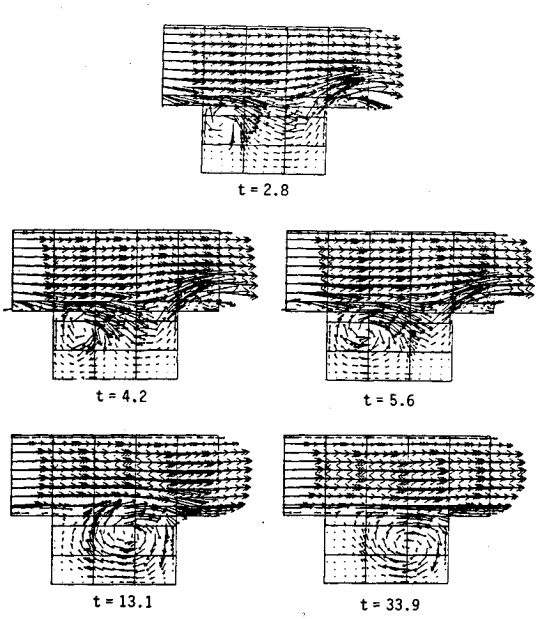

Fig. 2 Vector velocity plots of the starting flow at $R = 400$.

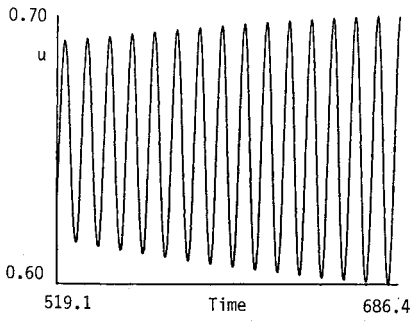

Fig. 3 Streamwise velocity u as a function of time at $R = 400$. The flow approaches a time-asymptotic oscillatory state of period $T = 11.1$.

are known from the nonlinear step calculations. Then, it can be written as a modified Helmholtz equation of the form

$$(\nabla^2 - m^2\beta^2)\Pi_m = g \quad m = 1, \ldots, M \quad \text{in } D \tag{23}$$

subject to homogeneous Dirichlet boundary conditions, $\Pi = 0$ on ∂D. Equation (23) is discretized using variational spectral elements in the x-y plane. The variational formulation recognizes the equivalence between solving the differential equation (23) and maximizing the functional

$$I_m(\Pi) = \int_D \left[-\frac{1}{2} \nabla \Pi_m \cdot \nabla \Pi_m - \frac{m^2\beta^2}{2}(\Pi_m)^2 - \Pi_m g \right] dA \tag{24}$$

The spectral element discretization corresponds to numerical quadrature of the variational form (24) restricted to the discrete space defined in terms of the parameters (K, N_1, N_2).

In local (r-s) coordinates, Eq. (24) is written as

$$I_m(\Pi) = \sum_{k=1}^{K} \int_{-1}^{1} \int_{-1}^{1} \left(-\frac{1}{2} \frac{\hat{\nabla}\Pi \cdot \hat{\nabla}\Pi}{|J|} - \frac{|J| m^2\beta^2}{2}\Pi^2 - |J|\Pi g \right) dr\, ds \tag{25}$$

where Π corresponds to Π_m, J is the Jacobian of the elemental transformations, and $\hat{\nabla}$ is the conservative form of the Jacobian multiplied gradient operator.[11]

To generate the discrete equations for each element k, we insert the interpolants (19) and the nodal collocation values of the geometric transformation into the functional (25). Then, we use a Galerkin-weighted residual technique and perform the resulting integrals, requiring stationarity at the collocation points. Using the selected Gauss-Lobatto Chebyshev collocation points ζ^k_{pq} and corresponding weights $\rho_{pq} = \rho_p \rho_q$, Eq. (25) is expressed as

$$\sum_{k=1}^{K} \sum_{p=0}^{N_1} \sum_{q=0}^{N_2} \rho_{pq} J^k_{pq} \left[\frac{\partial \Pi}{\partial x_j} \frac{\partial \Pi}{\partial x_j} \right]_{\zeta^k_{pq}} + m^2\beta^2 \sum_{k=1}^{K} \sum_{p=0}^{N_1} \sum_{q=0}^{N_2} \rho_{pq} J^k_{pq} [\Pi\, \Pi]_{\zeta^k_{pq}} = -\sum_{k=1}^{K} \sum_{p=0}^{N_1} \sum_{q=0}^{N_2} \rho_{pq} J^k_{pq} [\Pi\, g]_{\zeta^k_{pq}} \tag{26}$$

The Jacobian J^k_{pq} of the transformation from physical to local coordinates is calculated from the partial derivatives of the geometric isoparametric transformation r_x, r_y, s_x, and s_y.

Once the local basis function is selected, the spectral element approximation for Π^k is

$$\Pi^k = \sum_{n=0}^{N_1} \sum_{m=0}^{N_2} \Pi^k_{mn} h_m(r) h_n(s)$$
$$\forall_{m,n} \in (0, \ldots, N_1), \quad (0, \ldots, N_2) \tag{27}$$

where Π^k_{mn} are the expansion coefficients and also the local nodal values of Π. The geometry is also represented via similar tensorial products with same order polynomial degree, i.e.,

$$(x, y)^k = \sum_{n=0}^{N_1} \sum_{m=0}^{N_2} (x^k_{mn}, y^k_{mn}) h_m(r) h_n(s)$$
$$\forall_{m,n} \in (0, \ldots, N_1), \quad (0, \ldots, N_2) \tag{28}$$

where x^k_{mn} and y^k_{mn} are the global physical coordinates at the node (mn) in the k element.

To construct the discrete matrix of the global system, we insert Eq. (27) into Eq. (26) and perform direct stiffness summation,[12] adding at the boundary notes the contributions from the neighboring elements, obtaining

$$\sum_{k=1}^{K'} \sum_{m=0}^{N_1} \sum_{n=0}^{N_2} (\phi^k_{ijmn} + m^2\beta^2 J^k_{ij} B^k_{im} B^k_{jn}) \Pi^k_{mn} = -\sum_{k=1}^{K'} \sum_{m=0}^{N_1} \sum_{n=0}^{N_2} J^k_{ij} B^k_{im} \beta^k_{jn} g^k_{mn} \tag{29}$$

where Σ' denotes direct stiffness summation, and

$$\phi^k_{mn} = \rho_{pq} J^k_{pq} [(r_x)^2_{pq} \mathfrak{D}_{pi} \mathfrak{D}_{pm} \delta_{nq} + (s_x)^2_{pq} \mathfrak{D}_{qj} \mathfrak{D}_{qn} \delta_{mp} + (r_x s_x)_{pq} \mathfrak{D}_{pi} \mathfrak{D}_{qn} \delta_{mp} + (r_x s_x)_{pq} \mathfrak{D}_{qj} \mathfrak{D}_{qm} \delta_{nq}]$$

$$\mathfrak{D}_{ij} = \frac{\partial h_j}{\partial \zeta}(\zeta_i), \qquad B_{ij} = \int_{-1}^{1} h_i(\zeta) h_j(\zeta)\, d\zeta \qquad \zeta = r, s \tag{30}$$

The spectral solutions are C° across the boundaries of the elements with interfacial continuity constraints imposed only by the variational formulation without requiring any explicit patching at the elemental interfaces. Therefore, there is a weak coupling between dependent variables for neighboring elements. This results in banded, relatively sparse matrices, which are critical regarding computational efficiency of the method in terms of memory requirements and processing time.

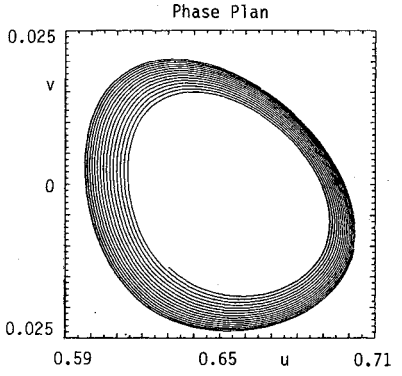

Fig. 4 Phase-plane portrait of v vs u velocities for the two-dimensional, self-sustained oscillatory flow.

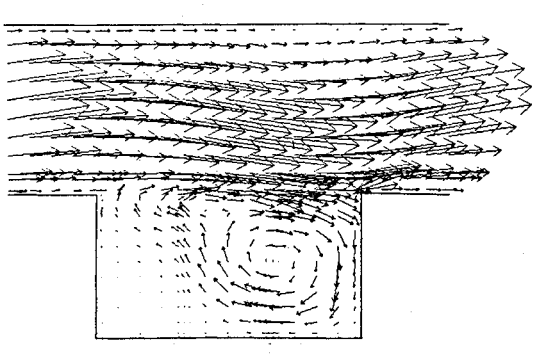

Fig. 5 Instantaneous velocity vector field at $R = 400$.

Assembly of the global matrix is done using parallel static condensation in which the nodes and their corresponding degrees of freedom are grouped into those lying on the boundary of the elements and those interior to an element. Then, the solution for the boundary nodes is decoupled from the solution for the interior nodes. This is an important feature because of the possibility of efficient implementation in parallel computer architecture.

The inversion of the global system matrix is carried out directly (LDL^T decomposition) in a preprocessing stage at the beginning of the simulation. Thereafter, only matrix multiplications are performed at each time step. Other implementations can use iterative techniques at each time step that usually require more computer time for a complete simulation but allow variable time steps and time-dependent fluid properties as well as moving boundaries.

The numerical calculations are performed employing 24 spectral elements using a 9×9 collocation grid in the x and y direction of each element and 16 Fourier expansions in the z direction. A typical three-dimensional run of 10,000 time steps takes about 16,180 CPU s on the Cray Y-MP/832.

IV. Results

In this section we present direct numerical simulations of two- and three-dimensional flows in periodic grooved channels as well as the linear evolution of instabilities arising from the interaction of three-dimensional disturbances with secondary two-dimensional flows. The grooved-channel geometry, shown in Fig. 1, corresponds to a nondimensional periodicity length $L/h = 5$, groove width $\ell/h = 3$, and groove depth $a/h = 1.68$. The transition simulation starts with a basic two-dimensional flowfield with superimposed, infinitesimally small disturbances consisting of three-dimensional Tollmien-Schlichting waves in the channel. The primary two-dimensional velocity field is obtained by direct numerical simulation of the two-dimensional Navier-Stokes equations starting with uniform velocity and evolving in time until a steady or time-periodic state is found.

Figure 2 shows the velocity vector plot of the startup flow at successive nondimensional time intervals from $t = 2.8$ to 33.9 at $R = 400$, where the flow is from left to right. Initially, a vortex forms in the upstream wall of the groove because of the separation at the abrupt channel expansion. This vortex entrains fluid from the channel to grow, move toward the downstream wall, and finally occupy the entire groove. The two-dimensional flow stabilizes with one primary vortex in the groove. Concurrently, the initial flat velocity profile in the channel part is evolving to a parabolic profile that is sensitive to Tollmien-Schlichting instabilities. Above a critical Reynolds number $R_{c,2D}$, these flows bifurcate from a steady to a two-dimensional, self-sustained oscillatory state.[6,13] For the grooved-channel geometry investigated in this paper, $R_{c,2D}$ is 320. These supercritical flows approach asymptotically a time-periodic state, as is shown in Fig. 3 by the history plot of the streamwise velocity as a function of time at a characteristic point of the domain at $R = 400$. This supercritical, two-dimensional secondary flow exhibits an oscillatory behavior approaching a limit cycle, shown in Fig. 4, in a phase-plane plot of v vs u velocity. The phase shift between the two components of the oscillatory velocity induces a Reynolds stress ($\rho \overline{u'v'}$) responsible for the increase in momentum diffusion, which converts energy from the basic mean flow to the oscillatory flow and sustains it. The period of the oscillation, nondimensionalized by the convective time, is $T = 11.1$, which coincides with the period of the Tollmien-Schlichting traveling waves corresponding to the least stable two-dimensional, Orr-Sommerfeld mode for plane Poiseuille flow. Similar self-sustained oscillatory flows at Tollmien-Schlichting frequencies were found in other modified channel geometries such as in channels with cylindrical promoters[13] and communicating channels.[14] The traveling wave structure of the resulting two-dimensional supercritical secondary flow is clearly depicted in Fig. 5 by a plot of the instantaneous velocity vectors. The flow pattern and vortex dynamics of these self-sustained supercritical flows show a very close resemblance with the one corresponding to subcritical, grooved-channel excitation.[15] In the latter, the flow is modulated at the frequency of the least-stable channel mode, whereas in the former, the flow achieves the oscillatory behavior spontaneously, induced and sustained by the periodic, geometric inhomogeneities of the grooves.

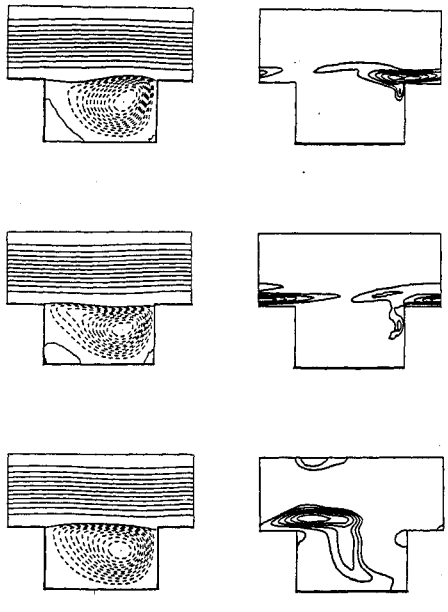

Fig. 6 Flow patterns in a sequence of three time frames within one period T at $R = 400$. Left: streamlines of the self-sustained oscillatory flow; right: iso-energy of the three-dimensional perturbations for $\beta = 2$.

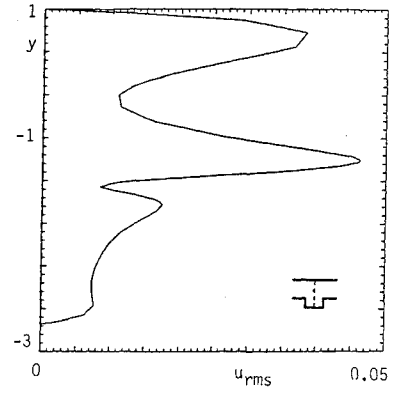

Fig. 7 Root-mean-square velocity profile at the groove center ($x/h = 2.5$, y/h).

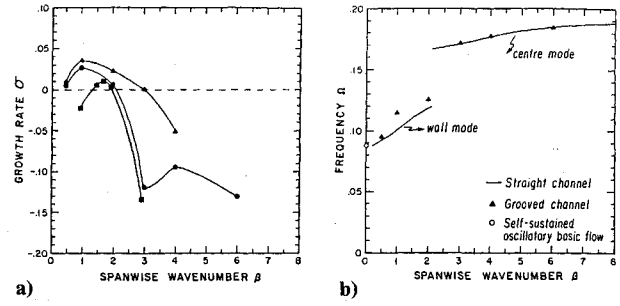

Fig. 8 a) Growth rate σ of the three-dimensional perturbation at $R = 350$ (■), $R = 400$ (•), and $R = 450$ (▲) as a function of β; b) dispersion relation for the grooved channel (▲) and plane-channel (–) flows at $R = 400$ and $\alpha = 1.2566$.

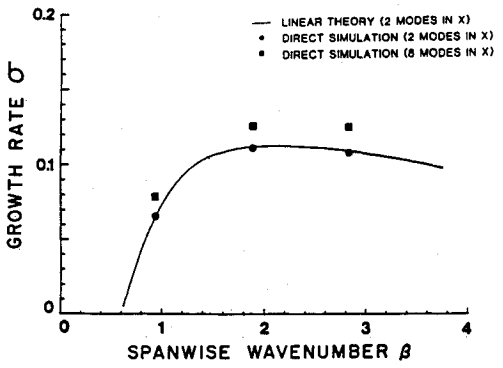

Fig. 9 Growth rate σ as a function of the wave number β for plane-channel flow.[18]

So far, from the two-dimensional simulations we have found a nonlinear saturation of the primary instability with the onset of a secondary periodic self-sustained supercritical flow for Reynolds numbers above $R_{c,2D}$. We investigate now the stability characteristics of these secondary flows by integrating simultaneously the full nonlinear two-dimensional Navier-Stokes equations and the three-dimensional linear perturbation equations until an asymptotic behavior is obtained. It is found that this two-dimensional grooved-channel flow is stable to any three-dimensional infinitesimal perturbation up to $R_{c,2D} = 340$ and unstable to a classical three-dimensional, secondary instability for $R > R_{c,3D} > R_{c,2D}$. Therefore, the primary instability at $R_{c,2D}$ leads to a nonlinear, two-dimensional secondary flow. Between the primary and secondary instability, the two-dimensional oscillatory flow is stable to all three-dimensional perturbations. In this range of Reynolds numbers, two-dimensional simulations are valid, and above $R_{c,3D}$, the effects of three-dimensionality need to be taken into account.

To get an overview of the transition development, we first consider the evolution of infinitesimally small perturbations of spanwise wave numbers β. Figure 6 shows the spatial distribution of the energy of the three-dimensional perturbed mode at three time instants in one cycle T of the secondary oscillatory flow at $R = 400$ and $\beta = 2$. It is verified that the intensity of the three-dimensional perturbation travels with the Tollmien-Schlichting wave. This implies that the source of the three-dimensional instability is the channel traveling waves, which suggests a classical, but detuned, channel secondary instability. It is interesting to note that the energy of the three-dimensional modes is concentrated in the bottom part of the grooved channel instead of being distributed in a staggered fashion as in plane-channel flow. To understand this feature, we plot in Fig. 7 the root-mean-square velocity profile of the secondary flow at the center of the groove. Aside from the groove shear layer, there are two critical layers in the channel, and the bottom critical layer is stronger and thinner. This suggests that the bottom critical layer, which is stronger because of proximity to the groove inhomogeneity, is mainly responsible for driving the three-dimensional instability.

The dependence of the growth rate σ on the spanwise wave number β of the infinitesimal three-dimensional perturbations is shown in Fig. 8a for different Reynolds numbers. It is seen that the secondary flow is unstable in a certain range of wave numbers β. The maximum value of σ indicates that the most unstable three-dimensional mode corresponds to a spanwise wave number β close to the streamwise wave number α. This implies that the most dangerous modes are at about 45 deg with respect to the mean flow. The grooved-channel flow exhibits a supercritical primary bifurcation where the amplitude of the stable, self-sustained secondary flow increases gradually from zero. Therefore, the three-dimensional growth-rate curve (Fig. 8a) rises above $\sigma = 0$ in a continuous and narrow-band fashion. As a result, spanwise modes are excited in a small range of β. The relatively low $R_{c,3D}$ insures that even in the case of positive growth the high wave number viscous cutoff restricts small-scale excitations.

Figure 8b shows the dispersion relation, that is, the three-dimensional perturbation frequencies as a function of β at $R = 400$ for the grooved and plane channels. It is verified that the frequency of the three-dimensional perturbation velocity does not lock with the self-sustained oscillatory flow. Instead, it is in closer agreement with the three-dimensional Tollmien-Schlichting mode of the same spatial structure (α, β), indicating that the dominant mechanism of frequency selection is determined by the channel part of the flow, which is the most stable component of the system. The discontinuity in the dispersion relation curve at $\beta = 2.25$ corresponds to a switch of the least-stable mode from a slow wall mode to a fast center mode. This exchange in modes has a drastic effect on the stability of the flow, with the center modes being significantly stabilized. Similar discrete jumps in frequencies have been observed experimentally[16] in oscillatory, separated flows in which the variation of a geometric parameter results in discrete frequency transitions.

To determine the effect of the groove inhomogeneity in the flow transition process, we compare the transition in the grooved channel with a plane channel that corresponds to a grooved-channel geometry with depth of the groove $a/h = 0$. The plane-channel flow presents a subcritical bifurcation[17] where the three-dimensional instability is born at the two-dimensional flow amplitude, which is significantly larger than that required for incipient growth. This leads to larger growth rates and, more importantly, to broadband spanwise excitation[18] as is shown in Fig. 9 by the plot of the growth rate σ vs spanwise wave number β. The broadband nature of the plane-channel instability is further amplified by the high Reynolds number associated with the primary bifurcation, since viscous effects play a less important role in stabilizing the flow.

The essential differences in the early transition and evolution of the instabilities in grooved and plane channels suggest that a different type of transition will occur. The low critical Reynolds number, the primary supercritical bifurcation,[19] and the narrow-band spanwise excitation in grooved-channel flows suggest that for Reynolds numbers above $R_{c,3D}$ a nonlinear three-dimensional, low-order equilibrium should exist. To demonstrate this, we integrate the full nonlinear, three-dimensional Navier-Stokes equations using as initial condition for the Fourier components of the velocities the three-dimensional linear perturbation modes. The direct numerical simulations indicate that this secondary instability saturates in a time-periodic, low-dimensional, tertiary equilibrium state, shown in Fig. 10a by the phase-plane portrait of the v velocity vs u velocity at $R = 350$. For larger Reynolds numbers, the flow can no longer be described by a small number of well-defined frequencies. This flow contains characteristics of both periodic and turbulent flow, as evidenced by the phase-plane portrait at $R = 425$ shown in Fig. 10b. Therefore, the transition to turbulence in the grooved-channel flow, shown in Fig. 1, develops through a sequence of bifurcations in contrast to plane-channel flow where the transition is of an abrupt type.

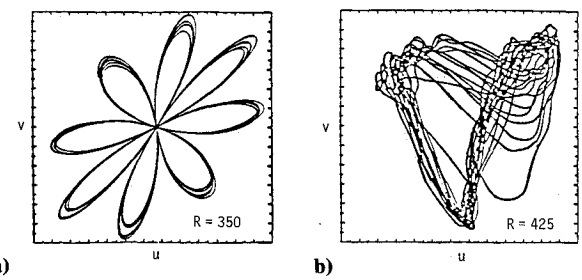

Fig. 10 Phase-plane portraits of v vs u velocities at a) $R = 350$ and b) $R = 425$.

As the Reynolds number is increased, the flow evolves and bifurcates from steady to two-dimensional, self-sustained oscillatory, then to three-dimensional quasiperiodic before manifesting any of the characteristics inherent to turbulent flow.

Acknowledgments

This work was supported by National Science Foundation Grants CTS-8909909 and EDC-8943164. I would like to thank A. T. Patera for helpful discussions and comments concerning this work.

References

[1]Orszag, S. A., and Kells, L. C., "Transition to Turbulence in Plane Poiseuille and Plane Couette Flows," *Journal of Fluid Mechanics,* Vol. 96, Jan. 1980, p. 159.

[2]Marcus, P. S., "Simulation of Taylor-Couette Flow," *Journal of Fluid Mechanics,* Vol. 146, Sept. 1984, p. 45.

[3]Pierrehumbert, R. T., and Widnall, S. E., "The Two- and Three-Dimensional Instabilities of a Spatially Periodic Shear Layer," *Journal of Fluid Mechanics,* Vol. 114, Jan. 1982, p. 59.

[4]Canuto, C., Hussaini, M. Y., Quarteroni, A., and Zang, T. A., *Spectral Methods in Fluid Dynamics,* Springer-Verlag, New York, 1987.

[5]Patera, A. T., "A Spectral Element Method for Fluid Dynamics," *Journal of Computational Physics,* Vol. 54, No. 3, 1984, p. 468.

[6]Amon, C. H., and Mikic, B. B., "Flow Pattern and Heat Transfer Enhancement in Self-Sustained Oscillatory Flows," AIAA Paper 89-0428, Jan. 1989.

[7]Amon, C. H., and Mikic, B. B., "Numerical Prediction of Convective Heat Transfer in Self-Sustained Oscillatory Flows," *Journal of Thermophysics and Heat Transfer,* Vol. 4, No. 2, 1990, p. 239.

[8]Karniadakis, G. E., and Amon, C. H., "Stability Calculations for Wall Bounded Flows in Complex Geometries," *Advances in Computer Methods for Partial Differential Equations VI,* edited by R. Vichnevetsky and R. S. Stepleman, International Assoc. for Mathematics and Computers in Simulations, New Jersey, 1987, p. 525.

[9]Boyd, J. P., "Chebyshev and Fourier Spectral Methods," *Lecture Notes in Engineering,* Springer-Verlag, Berlin, 1989.

[10]Deville, M., and Orszag, S. A., *Lecture Notes in Mathematics,* 1983, Vol. 771, Springer-Verlag, Berlin, 1980.

[11]Amon, C. H., "Heat Transfer Enhancement and Three-Dimensional Transition by a Spectral Element-Fourier Method," Sc.D. Thesis, Massachusetts Inst. of Technology, Cambridge, MA, 1988.

[12]Strang, G., and Fix, G., *An Analysis of the Finite Element Method,* Prentice-Hall, Englewood Cliffs, NJ, 1973.

[13]Karniadakis, G. E., Mikic, B. B., and Patera, A. T., "Minimum-Dissipation Transport Enhancement by Flow Destabilization: Reynolds' Analogy Revisited," *Journal of Fluid Mechanics,* Vol. 192, July 1988, p. 365.

[14]Amon, C. H., and Mikic, B. B., "Spectral Element Simulations of Unsteady Forced Convective Heat Transfer," *Numerical Heat Transfer,* Vol. 19, No. 1, 1991, p. 1.

[15]Ghaddar, N. K., Magen, M., Mikic, B. B., and Patera, A. T., "Numerical Investigation of Incompressible Flow in Grooved-Channels; Part 2: Resonance and Oscillatory Heat Transfer Enhancement," *Journal of Fluid Mechanics,* Vol. 168, July 1986, p. 541.

[16]Rockwell, D., "Prediction of Oscillation Frequencies for Unstable Flow Past Cavities," *Journal of Fluids Engineering,* Vol. 99, June 1977, p. 294.

[17]Herbert, T., "Secondary Instability of Plane Channel Flow to Subharmonic Three-Dimensional Disturbances," *Physics of Fluids,* Vol. 26, No. 4, 1983, p. 871.

[18]Orszag, S. A., and Patera, A. T., "Secondary Instability of Wall-Bounded Shear Flows," *Journal of Fluid Mechanics,* Vol. 128, March 1983, p. 347.

[19]Amon, C. H., and Patera, A. T., "Numerical Calculation of Stable Three-Dimensional Tertiary State on Grooved-Channel Flow," *Physics of Fluids A,* Vol. 1, No. 12, 1989, p. 2005.